

## Effect of trailing edge serration-flow misalignment on airfoil noise emissions

Arce León, Carlos; Merino-Martínez, Roberto; Ragni, Daniele; Avallone, Francesco; Scarano, Fulvio; Pröbsting, Stefan; Snellen, Mirjam; Simons, Dick G.; Madsen, Jesper

**DOI**

[10.1016/j.jsv.2017.05.035](https://doi.org/10.1016/j.jsv.2017.05.035)

**Publication date**

2017

**Document Version**

Accepted author manuscript

**Published in**

Journal of Sound and Vibration

**Citation (APA)**

Arce León, C., Merino-Martínez, R., Ragni, D., Avallone, F., Scarano, F., Pröbsting, S., Snellen, M., Simons, D. G., & Madsen, J. (2017). Effect of trailing edge serration-flow misalignment on airfoil noise emissions. *Journal of Sound and Vibration*, 405, 19-33. <https://doi.org/10.1016/j.jsv.2017.05.035>

**Important note**

To cite this publication, please use the final published version (if applicable).  
Please check the document version above.

**Copyright**

Other than for strictly personal use, it is not permitted to download, forward or distribute the text or part of it, without the consent of the author(s) and/or copyright holder(s), unless the work is under an open content license such as Creative Commons.

**Takedown policy**

Please contact us and provide details if you believe this document breaches copyrights.  
We will remove access to the work immediately and investigate your claim.

# Effect of trailing edge serration-flow misalignment on airfoil noise emissions

Carlos Arce León<sup>a,d,1,\*</sup>, Roberto Merino-Martínez<sup>c,1</sup>, Daniele Ragni<sup>d,2</sup>,  
Francesco Avallone<sup>d,3</sup>, Fulvio Scarano<sup>d,4</sup>, Stefan Pröbsting<sup>d,5</sup>, Mirjam  
Snellen<sup>c,6</sup>, Dick G. Simons<sup>c,4</sup>, Jesper Madsen<sup>b,7</sup>

<sup>a</sup>*LM Wind Power R&D, J. Duikerweg 15-A, 1703 DH Heerhugowaard, the Netherlands*

<sup>b</sup>*LM Wind Power, Denmark*

<sup>c</sup>*Aircraft Noise and Climate Effects, Delft University of Technology, Delft, the Netherlands*

<sup>d</sup>*Aerodynamics, Wind Energy, Flight Performance and Propulsion, Delft University of  
Technology, Delft, the Netherlands*

---

## Abstract

The broadband noise generated by the scattering of turbulent flow at the trailing edge of a NACA 0018 airfoil with trailing edge serrations is investigated varying both the airfoil angle of attack and serration flap angle. Acoustic emissions from the trailing edge are measured using a microphone array. The noise level is observed to be higher than that of the airfoil without serrations at frequencies beyond a crossover value. The latter is found to scale with a characteristic Strouhal number based upon the boundary layer thickness and the freestream velocity. A satisfactory collapse of the results under varying angles of attack and freestream velocities is observed. The modifications of the hydrodynamic behavior and the noise increase are linked by high-speed observations conducted with particle image velocimetry. An increase in the energy of turbulent fluctuations is also observed at the expected crossover frequency. The dominant cause of the increased noise is thereby identified at the pressure side edge of the

---

\*Corresponding author

*Email address:* caar@lmwindpower.com (Carlos Arce León)

<sup>1</sup>PhD candidate

<sup>2</sup>Assistant professor

<sup>3</sup>Postdoctoral researcher

<sup>4</sup>Full professor

<sup>5</sup>Guest researcher

<sup>6</sup>Associate professor

<sup>7</sup>Chief engineer

serrations at a given flap angle.

*Keywords:* aeroacoustics, trailing edge serrations, particle image velocimetry

---

## 1. Introduction

The scattering of surface pressure fluctuations at the airfoil trailing edge, driven by the turbulence in the boundary layer, becomes the most dominant source of airfoil self-noise at low Mach numbers ([1]). As a solution to mitigate this source of noise, serrated trailing edges have been proposed as a means to reduce the efficiency by which this scattering occurs. Models that predict the level of noise reduction have been suggested by [2, 3], and experimental proof of the noise reduction is provided in [4, 5, 6, 7]. The latter have observed reductions of up to 7 dB in wind tunnel measurements, in some contrast with the reduction levels predicted by [2, 8], which exceed 10 dB. Predictions by [3] yield noise reduction levels closer to those observed experimentally.

While noise reduction has been demonstrated consistently in wind tunnel measurements, an increase in noise beyond a certain frequency, called the crossover frequency, has also been observed ([4, 9, 10, 11, 12]). This departure is not foreseen in the analytical models proposed by [2, 8, 3], and has been ascribed to the increased turbulence intensity observed in the regions between serration teeth ([5]).

The increase is particularly evident when the serrated edge is not aligned with the undisturbed wake flow ([10]) due to a rotation about the  $z$  axis (see figure 1). This condition occurs when the airfoil is at incidence, and is even more pronounced when the serration has a flap angle ([13]). Although it can happen even at zero values of both if the airfoil has a camber that results in a flow curvature at the near-trailing edge wake. The condition in which the flow near the trailing edge is not aligned with the undisturbed freestream flow direction will be referred in the following as serration-flow misalignment. **In the present work, the degree of misalignment is given in terms of the angle of attack of the airfoil and the flap angle of the serrations.**

This condition is relevant in the industrial use of trailing edge serrations, such as in wind turbine blades. Situations which lead to a misalignment of the serration with respect to the undisturbed wake flow are common: the large range of angles of attack at which blade sections are operated, departures from the installation or manufacturing tolerances, and the prevalent use of cambered airfoils are a few examples. A certain level of misalignment must therefore be expected, and an investigation into how this causes the undesired increase in noise is essential.

The frequency above which this increase occurs is termed the crossover frequency,  $f_c$ , following [10]. It is correlated to the boundary layer thickness  $\delta_{99}$  (for simplicity contracted to  $\delta$ ) and the inflow velocity,  $U_\infty$ , through a constant Strouhal number

$$St_c = \frac{f_c \delta}{U_\infty}. \quad (1)$$

[10] proposed a value of  $St_c \approx 1$ . In [5] the boundary layer thickness parameter was approximated using  $\delta^*$  from XFOIL ([14]). This scaling behavior was found empirically from measurements of several serration geometries, retrofitted on a NACA 6512-10 airfoil, and run at flow velocities ranging from 20 to 70 m/s. The experimental measurements of  $St_c$  for the different cases collapse, with an uncertainty of 30%, around  $St_c = 1$ . [10] proposed a value of  $St_c \approx 1$ , found empirically from measurements of several serration geometries, retrofitted on a NACA 6512-10 airfoil, and run at flow velocities ranging from 20 to 70 m/s. Different angles of attack were also tested during this research, ranging from  $0^\circ$  to  $15^\circ$ , but it is not evident at which the results of the Strouhal number are discussed. The experimental measurements of  $St_c$  for the different cases collapse around  $St_c = 1$  with an uncertainty of 30%. The variance was attributed to the accuracy of the boundary layer estimation, which was not measured for all flow velocities, but was instead calculated using XFOIL. The authors further suggested that the collapse of  $St_c$  is expected to improve if spanwise variations of the boundary layer, introduced by the irregularity of the serrated edge, were to be considered.

Besides the pioneering work in [15, 5], and later [12], no other studies have tried to link the effect of serration misalignment to the important noise increase at high frequencies, despite its critical importance for the effective application of these devices in industrial settings. Moreover, detailed flow field measurements in addition to acoustic measurements are needed to provide insight into the origin of this effect.

Therefore, in order to confirm the observations in [15, 5] regarding the Strouhal number, and to further explore the relation between the hydrodynamic flow behavior and the noise increase, the present study employs a combination of acoustic microphone array measurements and flow field data obtained via particle image velocimetry.

A NACA 0018 airfoil, with its original straight trailing edge, and fitted with serrations, is experimentally tested at different freestream velocities. Multiple serration flap angles,  $\varphi$ , and angles of attack,  $\alpha$ , are prescribed as sources of serration-flow misalignment. Time-averaged flow information is obtained with stereoscopic particle image velocimetry (PIV, [16]), by which the boundary layer near the edge is studied. Its thickness is measured from the straight-edge airfoil and, with the acoustic measurements of  $f_c$ , the crossover Strouhal values are calculated.

Time-resolved PIV is then employed to inspect the flow dynamic behavior and reveal the link between the turbulent flow in the boundary layer and the far field acoustic spectra. In particular, parameters such as the streamwise length scales and most energy-bearing eddies are compared near the edge between the straight-edge and the serrated-edge airfoils. The turbulence frequency spectra are then used, in conjunction with the Strouhal number, to identify and locate the source of the high frequency noise increase.

## 2. Experimental setup

### 2.1. Flow facility, model, and flow conditions

Delft University of Technology’s vertical wind tunnel (V-Tunnel), with a square exit cross section of  $40\text{ cm} \times 40\text{ cm}$ , was used to carry out the experiments. Its freestream turbulence is reported to be below 1% at 10 m/s ([17]).

A NACA 0018 airfoil profile with a chord length  $C = 20\text{ cm}$  and span 40 cm, covering the full width of the test section, was selected. At the trailing edge, sawtooth serrations produced from a sheet of metal were attached. The tooth length was  $2h = 4.0\text{ cm}$  ( $0.2C$ ), the spanwise width was  $\lambda = 2.0\text{ cm}$  ( $\lambda = h$ ), and the thickness was equal to 1 mm. Figure 1 shows the airfoil, the dimensions of the serrations, and the coordinate system. The definitions of the angle of attack  $\alpha$  and the serration flap angle  $\varphi$  are also indicated. ~~The serration dimensions follow the recommendations in [5]. In particular, it is suggested that the length required to achieve a reduction in noise must comply with  $2h \gtrsim \delta$ , for  $\delta$  the boundary layer thickness. In the present case  $2h \approx 4\delta$  at  $\alpha = 0^\circ$ ,  $\varphi = 0^\circ$ .~~ The serration dimensions follow the recommendations in [5], where it is suggested that  $2h \gtrsim \delta$ , for  $\delta$  the boundary layer thickness. In the present case  $2h \approx 4\delta$  at  $\alpha = 0^\circ$ ,  $\varphi = 0^\circ$ .

Laminar-to-turbulent transition was forced with a strip of carborundum (nominal size of 0.6 mm) placed at  $0.2C$ , following guidelines given in [18], on both sides of the airfoil. The effectiveness of the device was verified using a remote microphone probe, which indicated a broadband spectrum in the turbulent boundary layer after transition.

Due to the change in slope at the junction between the airfoil and the serrated attachment, two coordinate systems are defined based on the wall-normal of the airfoil surface at the trailing edge and that of the serration surface. Figure 1 shows the coordinate system for the serrated attachment at  $\varphi = 0^\circ$  ( $x, y, z$ ) and for the airfoil ( $x', y', z$ ). For simplicity, the prime will be omitted in the results section and is implicit for the straight edged airfoil case. The velocity components corresponding to these coordinate systems will be indicated as  $(u, v, w)$ ,

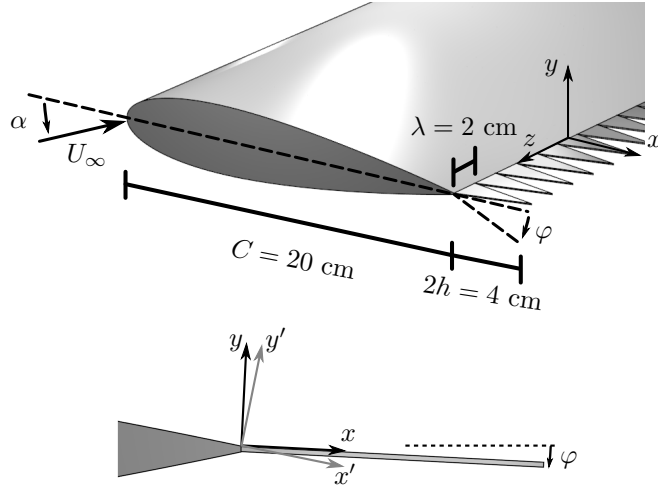


Figure 1: Airfoil and serration dimensions (top), and convention used for the coordinate system rotation over the airfoil and serration surfaces (bottom).

respectively, and are implied to be  $(u', v', w)$  for the airfoil measurements.

To investigate different levels of serration-flow misalignment, two serration flap angles and three angles of attack of the airfoil were selected. The flap angles tested were  $\varphi = 0^\circ$  and  $6^\circ$ , while the geometric values of the chosen angles of attack were  $\alpha_g = 0^\circ, 6^\circ$ , and  $12^\circ$ .

Both acoustic phased array and statistical flow field measurements with particle image velocimetry (PIV) were conducted spanning the range of flow velocities, 30, 35, and 40 m/s. The resulting chord-based Reynolds number is approximately 400,000, at the lowest velocity. This velocity range yields a sufficient signal-to-noise ratio for the trailing edge noise source above the laboratory background noise. The flow field measurements were conducted at a freestream velocity of 20 m/s, limited by the PIV system acquisition frequency and the temporal resolution necessary to obtain time-resolved flow information.

## 2.2. Acoustic measurements

Acoustic phased array measurements were recorded to estimate the noise modification due to the serrations. An array consisting of 64 microphones with an effective diameter of 0.9 m was used. The array configuration followed a planar multi-arm logarithmic spiral distribution ([19, 20]), as illustrated in figure 2. The array plane was parallel to the center plane of the wind tunnel and located at a distance of 1.05 m as illustrated in figure 3. The center of the array was aligned with the trailing edge of the airfoil at zero angle of attack. The test section was altered from the one described in the PIV setup by using longer side plates, which extended 0.7 m downstream of the airfoil trailing edge. The leading edge of the airfoil was located 0.5 m downstream from the nozzle exit. These modifications reduced the unwanted contribution of the parasitic noise sources due to the nozzle and the downstream edges of the side plates.

Every microphone in the array was calibrated before the experiment using a pistonphone. The performance of the array was evaluated with sound produced by a speaker at several discrete frequencies, and with white noise. The sound pressure level (SPL) values at the array center were also measured using a calibrated TENMA 72-947 sound level meter. Thus, the microphone array was calibrated for both source position and strength detection. Data was acquired at a sampling frequency of 50 kHz over a measurement period of  $T_{\text{meas}} = 60$  s. The acoustic data was averaged using time blocks of 2048 samples ( $\Delta t = 40.96$  ms) for each Fourier transform, and windowed by a Hanning weighting function with 50 % data overlap. After cross-correlating the microphones signals, the averaged cross-spectral matrix required for beamforming was obtained. With these parameters, the expected error ([21]) in the estimate of the cross-spectrum is:

$$\varepsilon_r = \sqrt{\frac{\Delta t}{T_{\text{meas}}}} = 2.6\%. \quad (2)$$

For applying beamforming to the data from acoustic phased array measurements, a scan grid of potential sound sources is defined. Conventional frequency

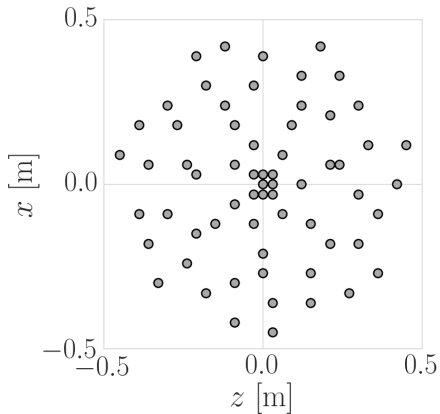


Figure 2: Microphone distribution within the array. Coordinates are shown in the coordinate system attached to the serrations at zero angle of attack.

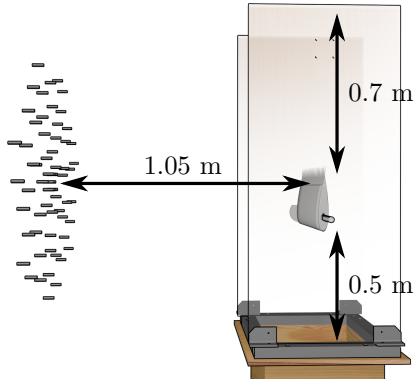


Figure 3: Schematic of the setup used for the acoustic measurements. The side plates are rendered here transparent.

domain beamforming ([22, 23]) is frequently applied for aeroacoustic measurements due to its simplicity, robustness and low computational demand. Unlike many deconvolution methods, this technique renders continuous results when applied to distributed sound sources, such as trailing edge noise ([24]). Therefore, conventional frequency domain beamforming was employed in the present study, considering a medium with uniform flow ([23]). The shear layer effect in the acoustic measurements ([25]) was assumed to be negligible due to the small angle ( $< 10^\circ$ ) between the array center, and the limits of the scanned area of interest and the considerably low flow speeds used ([26]). Source maps, also known as acoustic images, are obtained by applying the beamforming procedure for all the points in the scan grid. The scan grid covered a rectangle from  $z = -0.22$  m to  $z = 0.22$  m in the spanwise direction and from  $x = -0.3$  m to  $x = 0.3$  m in the streamwise direction, relative to the axes in figure 1, with a distance between grid points of 1 mm. Therefore, the scan grid contained the entire airfoil and was composed of  $441 \times 601$  grid points. Based on Rayleigh's criterion ([27]), the minimum resolvable distance for the highest frequency considered in this analysis (5 kHz), and considering  $c = 340$  m/s, is 0.10 m. The

considered spacing between grid points is approximately 100 times smaller than Rayleigh’s limit at 5 kHz.

Since trailing edge noise is expected to be a distributed sound source, the beamforming results were integrated over an area extending from  $z = -0.1$  m to  $z = 0.1$  m and from  $x = -0.06$  m to  $x = 0.06$  m (see figure 7). This area was selected to reduce the noise contribution from extraneous sources, while including a representative part of the trailing edge ([28]). The beamforming results in that area were normalized by the integral of a simulated unitary point source located at the center of the integration area evaluated within the same spatial domain ([23]). This process was repeated for each frequency of interest in order to obtain the trailing edge noise spectra.

### *2.3. Velocity measurements*

#### *2.3.1. Boundary layer characterization*

Boundary layer profiles and integral parameters for the straight trailing edge airfoil were obtained with low-repetition-rate planar PIV. The flow was seeded using an evaporated water-glycol based fog fluid (SAFEX), resulting in tracer particles of mean diameter below 1  $\mu\text{m}$ . A Quantel Twin BSL 200 laser (Nd:YAG, 200 mJ/pulse) was used for the illumination of these tracer particles in the measurement plane, which was oriented perpendicular to the airfoil surface and near mid-span ( $x$ - $y$  plane). Two PCO Sensicam QE CCD cameras with sensors of size  $1376 \times 1040$  px and a pixel-pitch of 6.7  $\mu\text{m}/\text{px}$  were used. Both cameras were equipped with Nikon NIKKOR macro objectives of 105 mm focal length and operated at an f-number of  $f/8$ . Their combined field of view (FoV) of  $36 \times 16$  mm<sup>2</sup> enclosed the boundary layer at the trailing edge at  $\alpha = 12^\circ$ . The resulting digital imaging resolution was approximately  $S = 65$  px/mm. Figure 4 shows a schematic of the setup. Sets of 300 uncorrelated image pairs were acquired per test case and camera at a frequency of 5 Hz and with a laser pulse separation time of  $\Delta t = 15$   $\mu\text{s}$ . At a freestream velocity of 20 m/s, this pulse separation is equivalent to a freestream particle displacement of about  $\Delta x = 0.31$  mm, or  $S\Delta x = 20$  px.

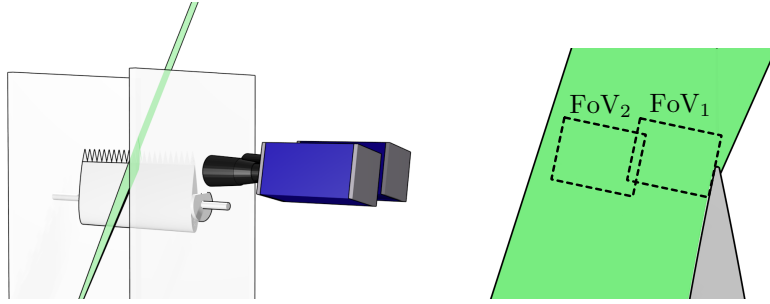


Figure 4: Planar PIV measurement setup (left) and resulting FoVs (right).

The acquired image pairs were processed with the LaVision DaVis 8 software using a multi-pass, multi-grid algorithm with window deformation ([29]). The final interrogation windows size was set to  $16 \times 16$  px and 50% overlap resulting in a physical interrogation window size of  $0.24 \times 0.24 \text{ mm}^2$  and vector spacing of  $0.12 \times 0.12 \text{ mm}^2$ . Uncertainty in the vector fields, at this magnification and flow conditions, is typically driven by cross-correlation uncertainty and peak-locking. With a relatively high magnification of 0.44 and a pixel-pitch of  $6.7 \text{ }\mu\text{m}/\text{px}$ , peak-locking is unlikely since the particle image diameter exceeds one pixel ([30]). Uncertainty of the cross-correlation between the image pairs is the most critical source of random errors for the current setup. For 2-component, planar PIV, this error is typically estimated to be 0.1 px ([31]). Following this approach and with a freestream particle displacement of  $S\Delta x = 20$  px, the random error on the instantaneous velocity fields is estimated at 0.5% of the freestream velocity. For the given experimental setup and number of samples, the error on the mean velocity reduces to below 0.1% of the freestream velocity. Table 1 provides an overview of the experimental parameters for the statistical boundary layer measurements.

### 2.3.2. Time-resolved stereoscopic PIV

For the time-resolved flow field measurements, a stereoscopic PIV setup was employed to measure the temporal evolution and statistics of the three velocity components in the  $x$ - $y$  plane around the serrations. The flow was seeded

Table 1: Parameters for the boundary layer characterization PIV measurements.

Parameter	Symbol	Value
Sensor size		$1376 \times 1040$ px
Single field of view	SFoV	$20 \times 16$ mm <sup>2</sup>
Combined field of view	FoV	$36 \times 16$ mm <sup>2</sup>
F-number	$f/$	8
Focal length		105 mm
Magnification		0.44
Imaging resolution	$S$	65 px/mm
Laser pulse separation	$\Delta t$	15 $\mu$ s
Freestream displacement	$\Delta x$	$\approx 0.31$ mm
	$S\Delta x$	$\approx 20$ px
Light sheet thickness		1.5 mm
Acquisition frequency	$f_s$	5 Hz
Number of samples		300
Interrogation window size		$16 \times 16$ px
		$0.24 \times 0.24$ mm <sup>2</sup>
Vector spacing (overlap 50%)		$0.12 \times 0.12$ mm <sup>2</sup>

as described in the previous section. For illumination, a Quantronix Darwin Duo dual-cavity Nd:YLF high-speed laser was used ( $2 \times 25$  mJ at 1 kHz). Two high-speed Photron Fastcam SA1.1 CMOS high-speed cameras ( $1024 \times 1024$  px,  $20 \mu\text{m}/\text{px}$  pixel-pitch, 12 bit resolution) were equipped with 105 mm Nikon NIKKOR macro objectives set at an f-number of  $f/5.6$ . The cameras were placed such that the optical axis of the first camera was perpendicular to the measurement plane, while that of the second camera pointed upstream at a relative angle of  $35^\circ$  with respect to the first (see figure 5). With a field of view of  $26 \times 50 \text{ mm}^2$  (imaged with half the sensor:  $512 \times 1024$  px) centered on the serrated trailing edge (see figure 6), the digital image resolution was  $S = 20 \text{ px}/\text{mm}$  at a magnification of 0.4.

10,100 images were acquired at an effective repetition rate of 10 kHz (image pairs acquired at 5 kHz with  $\Delta t = 100 \mu\text{s}$ , corresponding to 10 kHz in single frame mode, s.f.), corresponding to a particle displacement of  $\Delta x = 1.25 \text{ mm}$  or  $S\Delta x = 25 \text{ px}$ . Additionally, 2000 image-pairs of particle images were acquired at 250 Hz in order to obtain time-uncorrelated statistics. The pulse separation was  $\Delta t = 50 \mu\text{s}$ , corresponding to a freestream particle displacement of  $\Delta x = 0.6 \text{ mm}$  or  $S\Delta x = 12.5 \text{ px}$ .

LaVision DaVis 8 was used for image acquisition and processing. For both configurations, a multi-pass stereoscopic cross-correlation was applied with a final interrogation window size of  $16 \times 16 \text{ px}$  and an overlap factor of 75%, resulting in a spatial resolution of 0.8 mm and a vector spacing of 0.2 mm. Conventional stereoscopic calibration and self-calibration alleviated aspects such as lens distortion and resulted in a disparity vector of less than 0.1 px. This is considered sufficient for stereoscopic cross-correlation ([31]). Table 2 provides an overview of the experimental parameters for the boundary layer measurements.

At the given magnification factor of about 0.4, the particle image diameter is about  $10 \mu\text{m}$  ([30]). Mitigation of the peak-locking effect by defocusing was verified by considering the histogram of the particle displacements. All measured

---

<sup>8</sup>Single frame

Table 2: Parameters for the time-averaged and time-resolved stereoscopic PIV measurements.

Parameter	Symbol	Acquisition	
		Statistical	Time-resolved
Sensor size		$512 \times 1024$ px	$512 \times 1024$ px
Field of view	FoV	$26 \times 51$ mm <sup>2</sup>	$26 \times 51$ mm <sup>2</sup>
F-number	$f/$	5.6	5.6
Focal length		105 mm	105 mm
Magnification		$\approx 0.4$	$\approx 0.4$
Imaging resolution	$S$	20 px/mm	20 px/mm
Interrogation window size		$16 \times 16$ px	$16 \times 16$ px
		$0.8 \times 0.8$ mm <sup>2</sup>	$0.8 \times 0.8$ mm <sup>2</sup>
Vector spacing (overlap 75%)		$0.2 \times 0.2$ mm <sup>2</sup>	$0.2 \times 0.2$ mm <sup>2</sup>
Laser pulse separation	$\Delta t$	50 $\mu$ s	100 $\mu$ s
Freestream displacement	$\Delta x$	$\approx 0.6$ mm	$\approx 1.25$ mm
	$S\Delta x$	$\approx 12$ px	$\approx 25$ px
Light sheet thickness		1.5 mm	1.5 mm
Acquisition frequency	$f_s$	250 Hz	5 kHz (10 kHz) <sup>8</sup>
Number of samples		2000	10.100

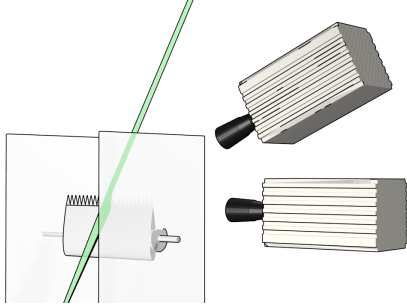


Figure 5: Stereo PIV measurement setup.

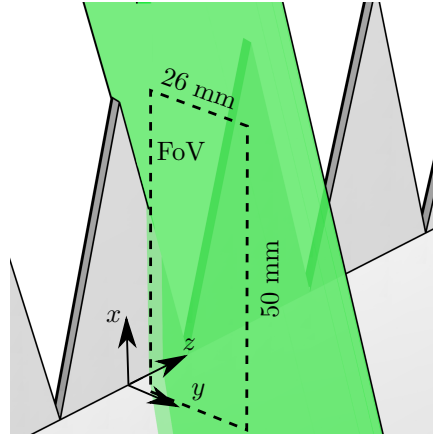


Figure 6: Location of the field of view for the stereoscopic PIV measurements in the  $z/\lambda = 0.25$  measurement plane.

velocity values,  $n_i = U_i - [U_i]$ , with the floor function  $[\cdot]$ , were distributed within 0.95 and 1.07 of  $n_i/\bar{n}_i$ , confirming the small effect of peak-locking in the measurement uncertainty. More important is the filtering effect due to the spatial resolution. With the application of the aforementioned multi-pass cross-correlation algorithm and window deformation, it has been established by [32] that the velocity amplitude modulation will vary with less than 5% for windows smaller than 0.6 times the characteristic wavelength. In the present case, a window size of  $0.8 \times 0.8 \text{ mm}^2$  was obtained, therefore allowing the measurement of flow structures down to 1.2 mm with 95% accuracy. In order to quantify random errors encountered in the present PIV setup, an *a-posteriori* statistical method, introduced by [33], was used. Following [33], the random error in each velocity field is approximately 1% in the freestream, and around 3% in the inner boundary layer. As a consequence, for the acquired number of samples (2000), the resulting error in the mean velocity is within 0.05% and 2% for the root-mean-square (rms) value.

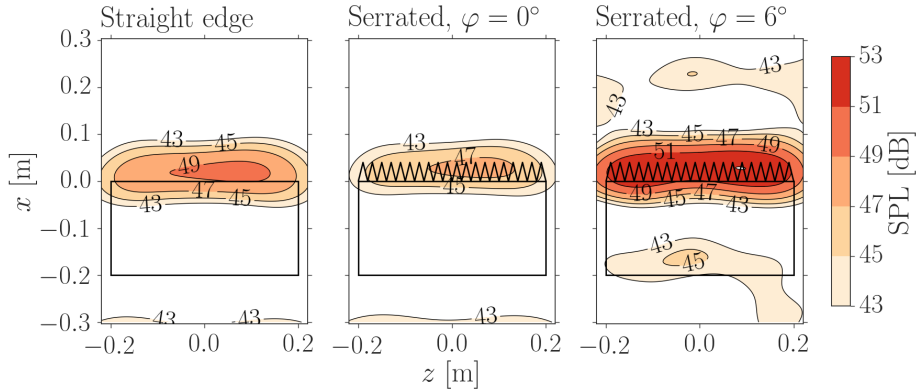


Figure 7: Acoustic source maps for a third-octave band center frequency of 4 kHz. Airfoil with straight trailing edge (left), serrated trailing edge with  $\varphi = 0^\circ$  (center), and  $\varphi = 6^\circ$  (right). Thin lines indicate the airfoil and the serrations.  $U_\infty = 35$  m/s,  $\alpha = 0^\circ$

### 3. Results

#### 3.1. Acoustic emissions

The acoustic measurements yield the difference in the acoustic frequency spectra between the original and the serration-retrofitted trailing edge. Figure 7 shows the acoustic source maps for the baseline configuration and the serrated trailing edges, with  $\varphi = 0^\circ$  and  $6^\circ$ , at a third-octave band center frequency of 4 kHz. The data shown was acquired at  $U_\infty = 35$  m/s and  $\alpha = 0^\circ$ . The trailing edge of the airfoil (indicated by the thin line) poses the primary sound source in all three cases. The flow-aligned serrations provide a noise reduction of about 2 dB, while the flow-misaligned serrations ( $\varphi = 6^\circ$ ) have an adverse effect.

The plots in figure 8 show the integrated third-octave band SPL with  $\alpha$  varying between  $0^\circ$  and  $12^\circ$ , and for  $\varphi = 0^\circ$  and  $6^\circ$ , respectively. The serrations are seen to effectively lower the noise emission when compared to the original edge geometry, as also observed in [5, 6, 11]. The fact that the reduction is also present at low frequency is consistent with the aforementioned studies. Cases with  $\varphi = 0^\circ$  exhibit a noise reduction of about 7 dB at  $f \approx 1$  kHz. At higher frequency, the noise reduction decreases, resulting in very similar levels for both configurations at 5 kHz. Serrations with  $\varphi = 6^\circ$  also reduce the noise by about

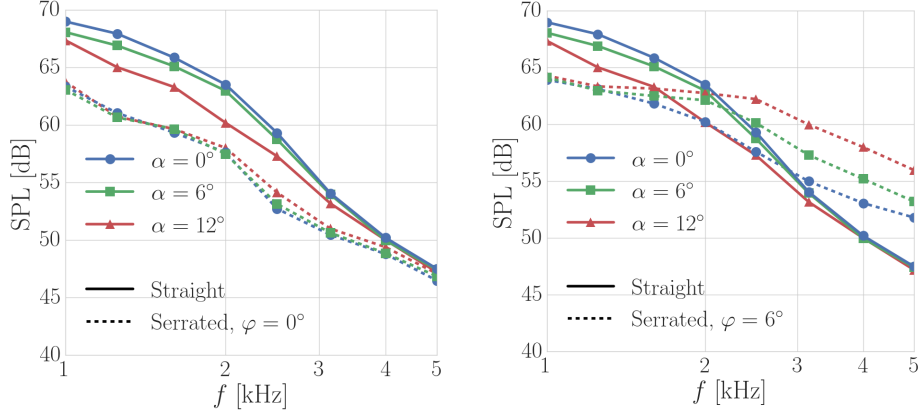


Figure 8: Third-octave band SPL for the straight and serrated trailing edges for various  $\alpha$ .  $U_\infty = 35$  m/s,  $\varphi = 0^\circ$  (left) and  $\varphi = 6^\circ$  (right).

5 dB at the low frequency, but the flatter spectrum leads to its intersection with that of the baseline trailing edge at about  $f_c = 3.0$  kHz. The frequency where the crossover takes place varies with the airfoil incidence:  $f_c = 3.0$  kHz, 2.2 kHz, and 1.6 kHz, respectively for the cases  $\alpha = 0^\circ$ ,  $6^\circ$  and  $12^\circ$ .

As shown for  $U_\infty = 35$  m/s in figure 8, crossover frequencies are only observed for  $\varphi = 6^\circ$ , but regardless of  $\alpha$ . The same holds for the tests conducted at  $U_\infty = 30$  and 40 m/s, which are omitted for sake of conciseness. This behavior is ascribed to the effect of the near-surface mean flow deflection and the formation of streamwise coherent structures. In [13] it is argued that changes in the angle of attack induce a global deformation of the flow field around the airfoil and shows that a flap angle induces instead a localized effect, along with a change of the local pressure gradient and turbulence intensity. This supports the hypothesis that the noise increase is due to the serration misalignment with the flow, leading to an increase in turbulence levels near the edge.

To facilitate the comparison between the emissions from the serrated edge and the baseline configuration for the representative case  $\varphi = 6^\circ$ , differences in SPL are presented in figures 9a, 9b, and 9c for  $\alpha = 0^\circ$ ,  $6^\circ$ , and  $12^\circ$ , respectively. Positive values indicate a reduction in noise. The crossover frequency is estimated by linear interpolation of the third-octave band data.

Figure 9a shows the results for  $\alpha = 0^\circ$ , where the serrations exhibit a similar reduction in noise between the three measured velocities, at around  $f = 1$  kHz ( $\Delta\text{SPL} = 5$  dB). The amount of reduction quickly decreases as the frequency increases, which occurs earlier for lower velocities. At the highest frequencies measured and  $U_\infty = 30$  m/s, serrations attain a noise level 5 dB louder than the straight trailing edge. For  $\alpha = 6^\circ$ , as discussed above (figure 9b), the crossover frequency is lower than for  $\alpha = 0^\circ$  at all measured velocities. The difference in SPL at the lower frequency is between 4 and 5 dB, while at  $f = 5$  kHz the increase in SPL reaches 7.5 dB. A similar result is seen for  $\alpha = 12^\circ$ , where crossovers occur at even lower frequencies, between  $f_c = 1.5$  kHz and 1.8 kHz. In this case, the increase in SPL at the highest measured frequency,  $f = 5$  kHz, reaches a value of around 8 dB.

### 3.2. Crossover frequency scaling

Different boundary layer thickness parameters were investigated in order to evaluate their effect on  $\text{St}_c$  (Eq. (1)) and its collapse: the wall-normal location of the  $0.99 u_e$  velocity (where  $u_e$  is the edge velocity of the boundary layer),  $\delta_{99}$ , the displacement thickness,  $\delta^*$ , and the momentum thickness,  $\theta$ . In contrast to [5], the edge velocity  $u_e$  was considered as the velocity scale.

The boundary layer parameters were evaluated over the straight airfoil trailing edge, following the aforementioned study. Figure 10 shows the different boundary layer parameters for various angles of attack and freestream velocities. The parameters generally show an increasing trend with angle of attack on the suction side and a decreasing trend on the pressure side. A larger variation between the different velocities is observed with increasing angle of attack, especially noticeable on the suction side. It is worth to note that  $\delta^*$  shows a larger relative increase with an increase in angle of attack.

Based on the boundary layer parameters in figure 10,  $\text{St}_c$  was evaluated using the crossover frequencies for the serrated edge at  $\varphi = 6^\circ$  discussed in section 3.1. Figures 11 and 12 show  $\text{St}_c$  obtained using the suction and pressure side boundary layer parameters, respectively. In both cases, the crossover frequency

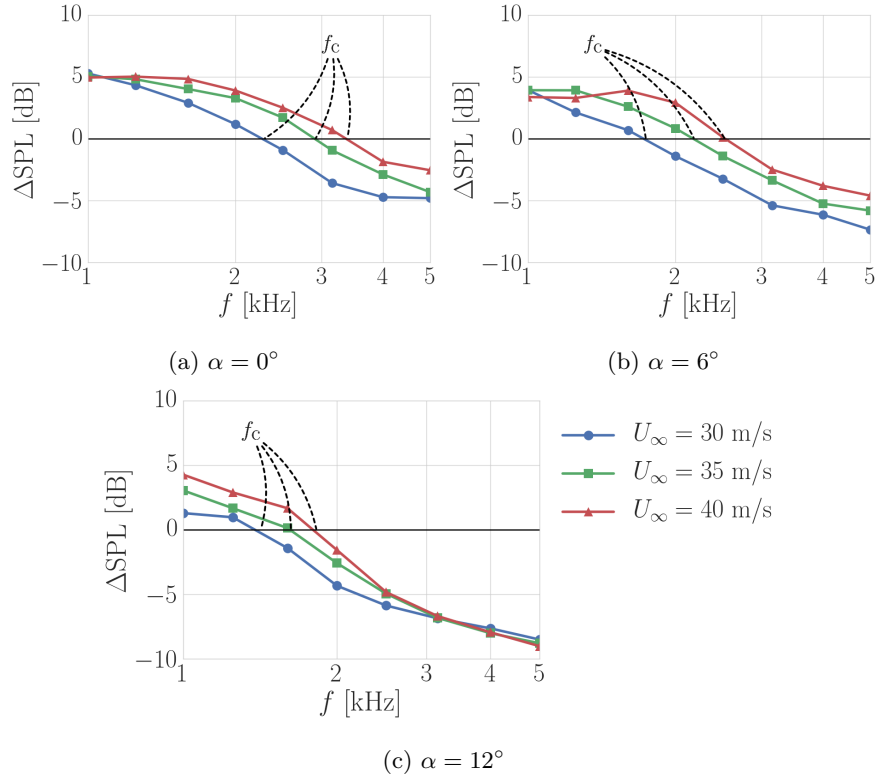


Figure 9: Noise reduction for the serrated trailing edge relative to the baseline airfoil for different  $\alpha$  values and  $\varphi = 6^\circ$ . The crossover frequency  $f_c$  is indicated for each  $U_\infty$ .

$St_c$  generally collapses well within 10% varying the freestream velocity.

When considering different angles of attack, a constant Strouhal number cannot be identified. This suggests that the latter, as hypothesized in [10], is valid for changes in the freestream velocity at an identical level of airfoil incidence. A linear trend in  $St_c$  is nevertheless found for different angles of attack, indicated by the linear regression applied to the measured data in figures 11 and 12 (dashed line). ~~To evaluate the quality of this fit, its~~ In order to quantify the predictability of the data with the given linear trend over the three velocities presented, the coefficient of determination,  $r^2$ , is indicated in figures 11 and 12.

With  $\delta_{99}$  as the characteristic length scale over the suction side (figure 11,

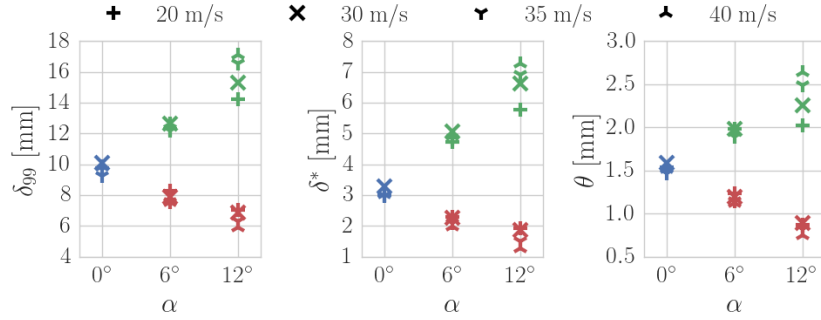


Figure 10:  $\delta_{99}$ ,  $\delta^*$  and  $\theta$ , at the trailing edge of the baseline airfoil.  $U_\infty = 20$  m/s: +,  $U_\infty = 30$  m/s:  $\times$ ,  $U_\infty = 35$  m/s:  $\gamma$ ,  $U_\infty = 40$  m/s:  $\lambda$ . Pressure side (red), suction side (green), and measurements at  $\alpha = 0^\circ$  (blue).

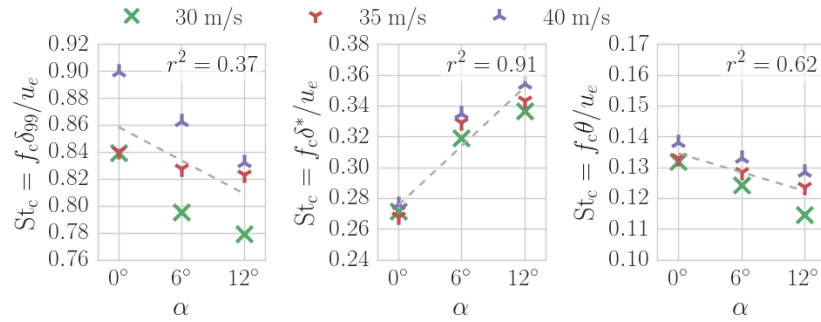


Figure 11:  $St_c$  for different boundary layer thickness parameters measured on the suction side.  $U_\infty = 30$  m/s:  $\times$ ,  $U_\infty = 35$  m/s:  $\gamma$ ,  $U_\infty = 40$  m/s:  $\lambda$ .

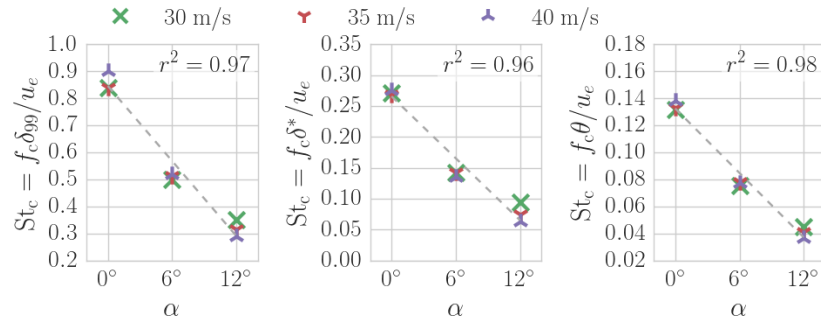


Figure 12:  $St_c$  for different boundary layer thickness parameters measured on the pressure side.  $U_\infty = 30$  m/s:  $\times$ ,  $U_\infty = 35$  m/s:  $\gamma$ ,  $U_\infty = 40$  m/s:  $\lambda$ .

left),  $St_c$  on one hand shows a decreasing trend with increasing  $\alpha$ . On the other hand, the values exhibit a large spread for the different velocities. With  $\delta^*$  (figure 11, center),  $St_c$  instead shows an increase for increasing  $\alpha$ . This results in the aforementioned larger relative increase in  $\delta^*$  (figure 10, center). Overall, the collapse of  $St_c$  with respect to the fit is very good when different values of the freestream velocity are considered (maximum 10% deviation for the suction side with  $\delta_{99}$ ). The variation of  $St_c$  with  $\theta$  (figure 10, right) is similar to that with  $\delta_{99}$  and shows a downward trend with increasing  $\alpha$ . In conclusion, the scaling with the displacement thickness,  $\delta^*$ , offers a more systematic fit with the data.

In general, the results suggest that a universal collapse of  $St_c$  for all angles of attack and Reynolds numbers is not possible with the set of scaling parameters investigated here. On the pressure side,  $St_c$  appears to vary with near-linear behavior with angle of attack, exhibiting consistently high values of  $r^2$  over the three boundary layer thickness parameters. ~~whereas the suction side~~ The suction side, on the other hand, has a less predictable behavior, exhibiting  $r^2$  of 0.37, 0.91 and 0.62. While the parameters used for scaling of the crossover Strouhal number were measured on the baseline airfoil, they are indicative of the condition when the serration is applied.

### 3.3. Near-edge flow characterization

PIV measurements in the  $x$ - $y$  plane are used to characterize the mean flow and turbulence intensity in the near-edge boundary layer. The analysis will compare key parameters between the straight edge and the serrated edge. The angle of attack and serration flap angle used are  $\alpha = 12^\circ$ ,  $\varphi = 6^\circ$ , at a freestream velocity of  $U_\infty = 20$  m/s. As stated in section 2, this is the upper velocity limit at which good-quality time-resolved flow information was obtainable with the current PIV system. The  $\alpha = 0^\circ$ ,  $\varphi = 0^\circ$  case is additionally shown for comparison. This configuration was chosen based on the predicted value of  $f_c$  for this case, which is expected to occur well below the upper frequency limit of the time-resolved flow data. Its approximation is discussed further below.

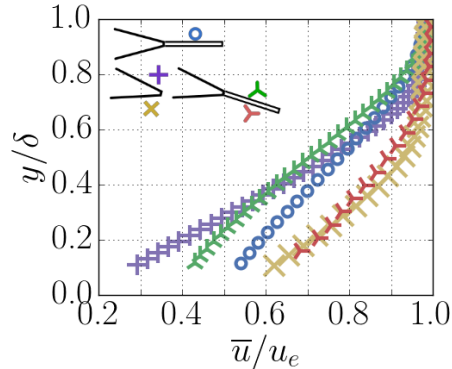


Figure 13: Streamwise mean flow component,  $\bar{u}$ .

The analysis is performed by comparing the flow at the serration edge at the plane crossing  $z/\lambda = 0.25$  (as indicated in section 2.3 and figure 6) and  $x/2h = 0.5$ , with the flow over the straight edge of the unserrated airfoil at  $x/2h = 0$ . The choice of this location has been made based on results from [13]. It is established there that, at this location over the serrated edge, the flow experiences the largest degree of spanwise flow deflection near the edge when serration-flow misalignment is prescribed.

The mean flow component in the streamwise direction,  $\bar{u}$ , is presented in figure 13. Suction and pressure side measurements are shown for the straight and the serrated edges at  $\alpha = 12^\circ$ , with  $\varphi = 6^\circ$  for the latter. Additionally, the serrated edge in the flow-aligned configuration,  $\alpha = 0^\circ$ ,  $\varphi = 0^\circ$ , is shown for reference.

On the pressure side trailing edge, both the straight and serrated airfoil edges exhibit higher velocity than at the suction side. Values of  $\bar{u}$  for  $\alpha = 0^\circ$ ,  $\varphi = 0^\circ$  are found between those observed for the suction and pressure sides for the serrated  $\alpha = 12^\circ$ ,  $\varphi = 6^\circ$  case. The lower speed over the suction side is due to the adverse pressure developing with the airfoil incidence. These results also confirm that no region of reverse flow is formed at the suction side.

As mentioned above, the largest degree of flow deflection is experienced at this edge location for the flow-misaligned serrations ( $z/\lambda = 0.25$ ,  $x/2h = 0.5$ ).

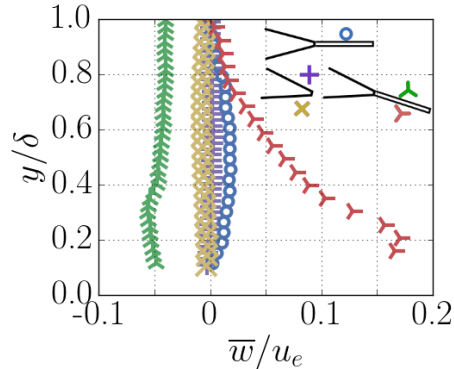


Figure 14: Spanwise mean flow component,  $\bar{w}$ .

To quantify this, figure 14 presents the profile of the spanwise mean velocity component,  $\bar{w}$ . When the mean flow is not significantly modified, such as in the case of the straight edge, and when the serrations are flow-aligned,  $\bar{w}$  is close to zero.

Misaligned serrations instead exhibit a significant spanwise velocity of  $\bar{w} \approx 0.15 u_e$ . The highest level of deflection occurs on the pressure side, at around  $y/\delta \approx 0.2$ , with a quick decrease away from the wall, and reaches  $\bar{w} = 0$  the edge of the boundary layer. Therefore, the spanwise flow deflection has an effect on the entire boundary layer flow. On the suction side, the deflection is about a third of that of the pressure side,  $\bar{w} \approx 0.05 u_e$ , with opposite direction (towards the center of the serration tooth). It has a rather uniform value due to the effect of the streamwise vortex formed behind the serration, as discussed in [34, 13].

The mean wall-normal flow component,  $\bar{v}$ , is shown in figure 15. Here, negative values represent flow that is oriented towards the surface (it is reminded that the  $y$  axis is chosen such that it is always wall-normal). As expected, the surface at the pressure side of the flow-misaligned serration experiences a considerable degree of flow directed towards the wall. This suggests that an efficient transfer of energy from the turbulent eddies to the unsteady surface pressure is expected in this region. This likely results in a significant contribution to the noise produced by the edge. The same measurement over the suction side shows

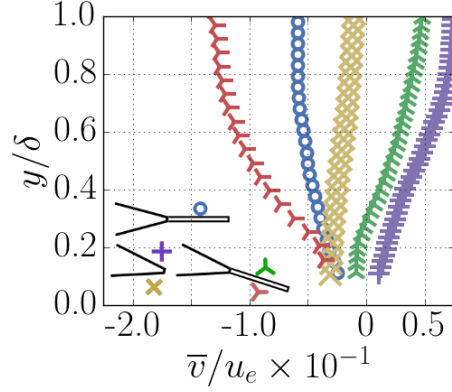


Figure 15: Wall-normal mean flow component,  $\bar{v}$ .

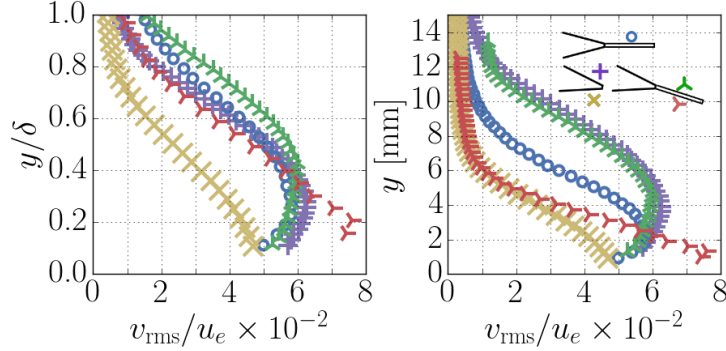


Figure 16: Wall-normal fluctuations,  $v_{\text{rms}}$ .

instead flow being directed away from the wall, a consequence of the flow passing through the serration teeth. Due to the nature of the serration geometry, with its angled edge, the streamwise vortex that is being formed behind it fails to impinge on its suction side surface, contrary to what is usually observed in flap edges ([35]).

As the wall-normal component fluctuations,  $v_{\text{rms}}$ , are related to the increase in acoustic emissions by the edge (see the trailing edge noise prediction equations in [36, 2, 37], where the flow turbulence spectrum drives the produced sound), they are here investigated. Figure 16 (left) shows similar behavior and levels for the suction side measurements, reaching maxima at about  $y/\delta = 0.3$ . While

the pressure side measurement of the straight edge airfoil shows the lowest values of  $v_{\text{rms}}$ , the measurement of the serrated edge airfoil exhibits instead a large increase near the surface, about a third larger than the maxima of the suction side measurements, and twice of the straight edge airfoil pressure side measurement. The results suggest a correlation between  $\bar{w}$  and  $v_{\text{rms}}$ , likely driven by the wall-normal transport of turbulent fluctuations as the streamwise vortex formation occurs.

The maximum of wall-normal fluctuations is observed at  $y/\delta = 0.2$  on the pressure side, which is considerably close to the wall (1.5 mm), noting that the boundary layer is significantly thinner here than on the suction side. The maxima for the suction side measurements occurs instead at around  $y = 5$  mm.

#### 3.4. Characterization of the near-edge time-resolved flow

The boundary layer thickness differences between the pressure and suction sides indicates a contraction of the integral length scale of the turbulent structures at the pressure side. This suggests that increased wall-normal fluctuations at the pressure side are due to smaller structures, contributing to the higher end of the noise frequency spectrum.

To evaluate this, the streamwise integral length scale is investigated, defined in [38] as

$$\Lambda_{x|uu} = \int_0^\infty R_{uu}(\xi_x) d\xi_x, \quad (3)$$

where  $\xi_x$  is the separation distance in the  $x$  direction between signals for the calculation of the spatial two-point correlation coefficient,

$$R_{uu} = \frac{\overline{u(x) \cdot u(x + \xi_x)}}{u^2(x)}. \quad (4)$$

As the upper boundary of the integral is limited by the field of view available, a fixed value is chosen for all the presented cases, such that  $\xi_{x,\text{max}} = 0.5h$ . The choice of  $\Lambda_{x|uu}$  over other scales comes from the ability to accurately describe it with the implemented measuring methodology. It scales linearly with  $\Lambda_{x|vv}$ , as shown by results in [38].

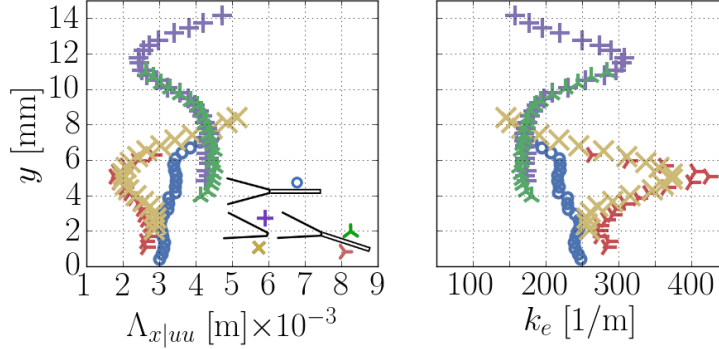


Figure 17: Streamwise turbulence length scale,  $\Lambda_{x|uu}$  (left), and most energetic streamwise wavenumbers (right).

Due to the angle of the serration surface against the mean flow direction, the latter is not necessarily parallel to the wall or the coordinate system arrangement used so far. A rotation in the axes has, therefore, been prescribed, such that the  $x$  direction is aligned with the local mean flow,  $\bar{u}$  (calculated *a-posteriori*), and the definition of  $\Lambda_{x|uu}$  is preserved. Some of the extent of  $\xi_{x,\max}$  is nevertheless lost due to this rotation, and the data is presented only for  $y$  locations where the limit  $0.5h$  is obtainable. The rotation is applied throughout the results presented in this section.

The values of  $\Lambda_{x|uu}$  are shown in figure 17, in terms of the absolute wall distance. Alongside are the values for the wavenumber of the most energy-bearing eddies, approximated empirically ([39]) as

$$k_e = \frac{\sqrt{\pi}}{\Lambda_{x|uu}} \frac{\Gamma(5/6)}{\Gamma(1/3)}, \quad (5)$$

where  $\Gamma$  is the gamma function.

A notable difference in the integral length scales between the pressure and suction side measurements is observed. The minimum wavelength on the pressure side is approximately 1.5 mm at around 5 mm distance from the wall. On the suction side, the minimum wavelength is 2.5 mm, detected at 11 mm from the upper surface. These observations support the argument that the pressure side contributes to the noise emission in the higher end of its frequency

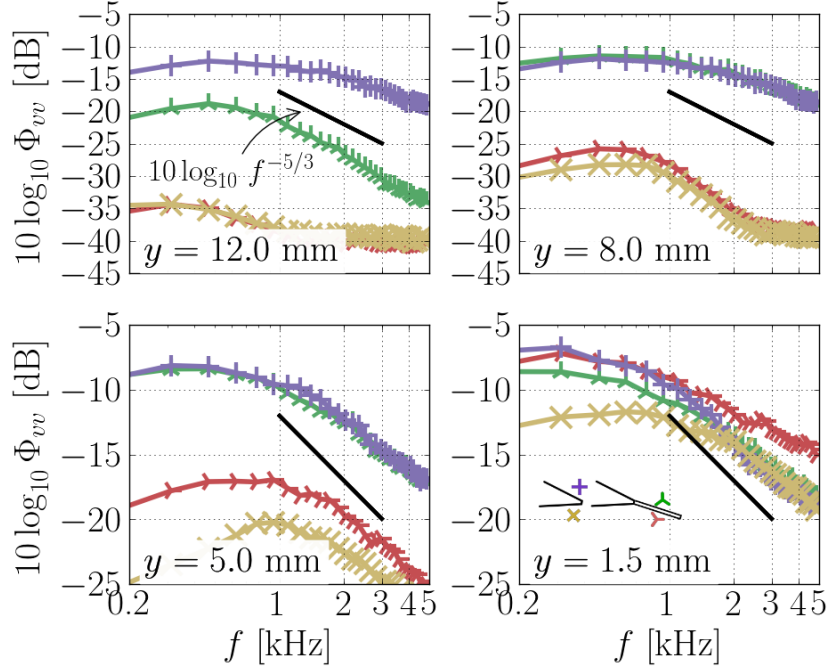


Figure 18: Spectrum of the wall-normal velocity component for different wall-normal locations.

spectrum.

A slightly higher wavenumber ( $k_e = 450 \text{ m}^{-1}$ ) is exhibited on the pressure side serrated case compared to the straight edge case ( $k_e = 370 \text{ m}^{-1}$ ), indicating a slight additional contraction of the boundary layer with the serration.

To illustrate the relation between the observed  $v_{\text{rms}}$  over the boundary layer and the energy in the turbulent flow eddies, the wall-normal flow component spectra,  $\Phi_{vv}$ , are presented in figure 18. The suction and pressure sides of the straight and serrated edges are presented for  $\alpha = 12^\circ$ ,  $\varphi = 6^\circ$ . The absolute wall-normal distance is used to present various locations in the boundary layer of each case, while maintaining the same wall distance scale. The Kolmogorov law is shown in the plots for reference. The signal floor due to noise is reached at about  $-40 \text{ dB}$ , as is evident from the plateau of the pressure side measurement.

The spectral results agree with the  $v_{\text{rms}}$  levels of the different cases. Larger values are observed over the straight edge at the location furthest from the wall,

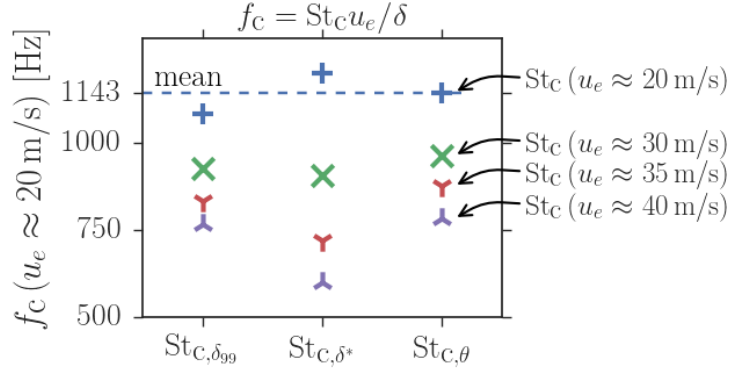


Figure 19: Predicted value of  $f_c$  based on the pressure side measurements of  $St_c$  based on  $U_\infty = 30$  m/s ( $\times$ ),  $U_\infty = 35$  m/s ( $\gamma$ ),  $U_\infty = 40$  m/s ( $\lambda$ ), and the linear extrapolation to  $U_\infty = 20$  m/s ( $+$ ).

$y = 12$  mm. The levels and spectral shape for the straight and serrated cases at  $y = 8$  mm are the same, as observed for  $v_{\text{rms}}$  at this location.

Nearer the wall, the pressure side cases exhibit increasing levels, by about 10 dB between  $y = 8$  and 5 mm. The most notable feature is found at  $y = 1.5$  mm, where the  $\Phi_{vv}$  levels of the pressure side reach those of the suction side. Most importantly, the levels for the pressure side of the serrated case exceed any other above roughly 1.1 kHz. A difference of around 5 dB is observed at the top limit of the observed frequency range.

The relation between this turbulence spectra crossover frequency and the acoustic spectrum one,  $f_c$ , will be here established. For this purpose, the value of  $f_c$  for this case,  $\alpha = 12^\circ$ ,  $\varphi = 6^\circ$  at 20 m/s, will be obtained with the  $St_c$  model, as discussed in section 3.2.

Each choice of  $\delta$  showed a dependence of  $St_c$  on  $u_e$ . Therefore, an estimation of  $f_c$  on  $u_e$  must take this into account. The results obtained in section 3.2 are linearly extrapolated to obtain the acoustic  $f_c$  for a 20 m/s freestream velocity. The result of

$$f_c = St_c u_e / \delta. \quad (6)$$

is shown in figure 19 for the freestream velocities of the acoustic measurements,

as presented in section 3.1, and the extrapolated result at 20 m/s PIV freestream velocity. The mean between the results of the different boundary layer thickness parameter results is indicated at 1.14 kHz, which correlates well to the observed crossover in the spectra of the turbulence  $\approx 1.1$  kHz.

These results confirm that the pressure side flow near the edge is the source of the high frequency noise increase, exhibiting a crossover value in the turbulence spectrum similar to that expected in the acoustic emissions.

#### 4. Conclusions

The increase in high frequency noise by trailing edge serrations has been confirmed using acoustic beamforming and ascribed to the misalignment of the serrations with regard to the otherwise undisturbed mean wake flow.

A Strouhal number, proposed by [5], relating the crossover frequency of the serration noise increase with the boundary layer thickness and its edge velocity, has been investigated. Contrary to a single-number collapse, it exhibits a linear modification with changes in angle of attack, and varies slightly for different freestream velocities. A better fit is furthermore found by taking the pressure, and not the suction side boundary layer thickness. As the thinner pressure side boundary layer carries smaller turbulent eddies, and in turn these relate to the production of higher frequency noise, its use in the Strouhal number calculation is more representative.

PIV measurements determine the boundary layer flow properties over the serration and straight trailing edge. A sharp increase in  $v_{\text{rms}}$  on the pressure side of the serrated case with a significant increase of spanwise velocity is observed. The integral length scale of the turbulence is retrieved, identified on the pressure side to be around half the size of the suction side values. This corresponds approximately to the pressure and suction side boundary layer thickness ratio.

The turbulence frequency spectrum exhibits an increase in energy corresponding to that of the estimated acoustic crossover. This increase is observed at the pressure side, where  $v_{\text{rms}}$  is seen to sharply increase, and coincides with

the highest spanwise flow deflection.

The latter suggests that the source of the high frequency noise leading to the crossover phenomenon is due to interactions taking place at the pressure side.

### Acknowledgments

The research of Carlos Arce León is funded by the Innovation Fund Denmark, Industrial PhD Programme project number 11-109522.

- [1] M. Howe, Trailing Edge Noise at Low Mach Numbers, *Journal of Sound and Vibration* 225 (2) (1999) 211–238. doi:10.1006/jsvi.1999.2236.  
URL <http://linkinghub.elsevier.com/retrieve/pii/S0022460X99922368>
- [2] M. S. Howe, Noise produced by a sawtooth trailing edge, *The Journal of the Acoustical Society of America* 90 (1) (1991) 482. doi:10.1121/1.401273.  
URL <http://link.aip.org/link/?JASMAN/90/482/1><http://scitation.aip.org/content/asa/journal/jasa/90/1/10.1121/1.401273>
- [3] B. Lyu, M. Azarpeyvand, S. Sinayoko, A Trailing-Edge Noise Model for Serrated Edges, in: 21st AIAA/CEAS Aeroacoustics Conference, AIAA, Dallas, Texas, 2015. doi:10.2514/6.2015-2362.  
URL <http://arc.aiaa.org/doi/10.2514/6.2015-2362>
- [4] T. Dassen, R. Parchen, J. Bruggeman, F. Hagg, Results of a wind tunnel study on the reduction of airfoil self-noise by the application of serrated blade trailing edges, Tech. rep., National Aerospace Laboratory, NLR (1996).
- [5] M. Gruber, P. Joseph, T. Chong, On the mechanisms of serrated airfoil trailing edge noise reduction, in: 17th AIAA/CEAS Aeroacoustics Conference (32nd AIAA Aeroacoustics Conference), Vol. 2781, American Institute of Aeronautics and Astronautics, Portland, Oregon, USA, 2011,

pp. 5–8. doi:10.2514/6.2011-2781.

URL <http://arc.aiaa.org/doi/pdf/10.2514/6.2011-2781>  
<http://arc.aiaa.org/doi/abs/10.2514/6.2011-2781>

- [6] D. Moreau, C. Doolan, Noise-Reduction Mechanism of a Flat-Plate Serrated Trailing Edge, *AIAA Journal* 51 (13) (2013) 2513–2522. doi:10.2514/1.J052436.

URL <http://arc.aiaa.org/doi/abs/10.2514/1.J052436>

- [7] C. Arce, D. Ragni, S. Pröbsting, F. Scarano, Flow Field Around a Serrated Trailing Edge at Incidence, in: 33rd Wind Energy Symposium, American Institute of Aeronautics and Astronautics, Kissimmee, Florida, 2015. doi:10.2514/6.2015-0991.

URL <http://arc.aiaa.org/doi/abs/10.2514/6.2015-0991>  
<http://arc.aiaa.org/doi/pdf/10.2514/6.2015-0991>

- [8] M. Azarpeyvand, M. Gruber, P. Joseph, An analytical investigation of trailing edge noise reduction using novel serrations, in: 19th AIAA/CEAS Aeroacoustics Conference, 2013.

URL <http://arc.aiaa.org/doi/pdfplus/10.2514/6.2013-2009>

- [9] S. Oerlemans, M. Fisher, T. Maeder, K. Kögler, Reduction of wind turbine noise using optimized airfoils and trailing-edge serrations, *AIAA Journal* 47 (6) (2009) 1470–1481. doi:10.2514/1.38888.

URL <http://doi.aiaa.org/10.2514/1.38888>

- [10] M. Gruber, P. Joseph, T. Chong, Experimental investigation of airfoil self noise and turbulent wake reduction by the use of trailing edge serrations, in: 16th AIAA/CEAS Aeroacoustics Conference, 2010, pp. 1–23.

URL <http://arc.aiaa.org/doi/pdf/10.2514/6.2010-3803>

- [11] A. Finez, E. Jondeau, M. Roger, M. C. Jacob, Broadband Noise Reduction of a Linear Cascade With Trailing Edge Serrations, in: 17th AIAA/CEAS

- Aeroacoustics Conference (32nd AIAA Aeroacoustics Conference), Portland, Oregon, USA, 2011. doi:10.2514/6.2011-2874.  
URL <http://arc.aiaa.org/doi/abs/10.2514/6.2011-2874>
- [12] A. Vathylakis, C. C. Paruchuri, T. P. Chong, P. Joseph, Sensitivity of aerofoil self-noise reductions to serration flap angles, 22nd AIAA/CEAS Aeroacoustics Conference (2016) 1–17doi:10.2514/6.2016-2837.  
URL <http://arc.aiaa.org/doi/10.2514/6.2016-2837>
- [13] C. Arce León, D. Ragni, S. Pröbsting, F. Scarano, J. Madsen, Flow topology and acoustic emissions of trailing edge serrations at incidence, *Experiments in Fluids* 57 (5) (2016) 91. doi:10.1007/s00348-016-2181-1.  
URL <http://link.springer.com/10.1007/s00348-016-2181-1>
- [14] M. Drela, XFOIL: An Analysis and Design System Low Reynolds Number Aerodynamics and Transition, *Lecture Notes in Engineering*, Springer Berlin Heidelberg, Berlin, 1989. doi:10.1007/978-3-642-84010-4.  
URL <http://www.springerlink.com/index/10.1007/978-3-642-84010-4>
- [15] M. Gruber, M. Azarpeyvand, P. F. Joseph, Airfoil trailing edge noise reduction by the introduction of sawtooth and slitted trailing edge geometries, *Proceedings of 20th International Congress on Acoustics, ICA 10 (August) (2010) 1–9*.  
URL [http://www.acoustics.asn.au/conference{}\\_proceedings/ICA2010/cdrom-ICA2010/papers/p686.pdf](http://www.acoustics.asn.au/conference{}_proceedings/ICA2010/cdrom-ICA2010/papers/p686.pdf)
- [16] M. P. Arroyo, C. A. Greated, Stereoscopic particle image velocimetry, *Measurement Science and Technology* 2 (12) (1991) 1181–1186. doi:10.1088/0957-0233/2/12/012.  
URL <http://iopscience.iop.org/article/10.1088/0957-0233/2/12/012>
- [17] S. Ghaemi, D. Ragni, F. Scarano, PIV-based pressure fluctuations in the turbulent boundary layer, *Experiments in Fluids* 53 (6) (2012) 1823–1840.

doi:10.1007/s00348-012-1391-4.

URL <http://link.springer.com/10.1007/s00348-012-1391-4>

- [18] A. L. Braslow, R. M. Hicks, R. V. Harris Jr., Use of grit-type boundary-layer transition trips on wind-tunnel models, NASA Technical Note (D-3579).

URL <http://ntrs.nasa.gov/search.jsp?R=19660026829>

- [19] T. Mueller, Aeroacoustic Measurements, Springer Science & Business Media, 2002, iSBN-978-3-642-07514-8.

URL <https://books.google.com/books?hl=en&lr=&id=MU6WLXFJLWgC&pgis=1>

- [20] S. Pröbsting, M. Zamponi, S. Ronconi, Y. Guan, S. C. Morris, F. Scarano, Vortex shedding noise from a beveled trailing edge, International Journal of Aeroacoustics 15 (8) (2016) 712–733. doi:10.1177/1475472X16666633.

URL <http://jae.sagepub.com/lookup/doi/10.1177/1475472X16666633>

- [21] A. Brandt, Noise and vibration analysis: signal analysis and experimental procedures, Second, John Wiley & Sons, 2011, ISBN 978-0-470-74644-8.

- [22] D. H. Johnson, D. E. Dudgeon, Array Signal Processing, Concepts and Techniques, P T R Prentice Hall, Englewood Cliffs, 1993, iSBN: 9780130485137.

- [23] P. Sijtsma, Phased array beamforming applied to wind tunnel and fly-over tests, Tech. Rep. NLR-TP-2010-549, National Aerospace Laboratory (NLR), Anthony Fokkerweg 2, 1059 CM Amsterdam, P.O. Box 90502, 1006 BM Amsterdam, The Netherlands (December 2010).

- [24] R. P. Dougherty, Functional Beamforming for Aeroacoustic Source Distributions, in: 20<sup>th</sup> AIAA/CEAS Aeroacoustics Conference. June 16-20 2014. Atlanta GA, USA., 2014, AIAA paper 2014-3066. doi:10.2514/6.

2014-3066.

URL <http://arc.aiaa.org/doi/pdf/10.2514/6.2014-3066>

- [25] R. Amiet, Correction of Open Jet Wind Tunnel Measurements For Shear Layer Refraction, in: *2<sup>nd</sup> AIAA Aeroacoustics Conference*, March 24-26, Hampton, VA, USA, 1975. doi:10.2514/6.1975-532.

URL <http://arc.aiaa.org/doi/pdf/10.2514/6.1975-532>

- [26] P. Salas, S. Moreau, Noise prediction of a simplified high-lift device, in: *22<sup>nd</sup> AIAA/CEAS Aeroacoustics Conference*. May 30 - June 1 2016. Lyon, France., 2016, AIAA paper 2016-2962. doi:10.2514/6.2016-2962.

URL <http://arc.aiaa.org/doi/pdf/10.2514/6.2016-2962>

- [27] F. R. S. Lord Rayleigh, XXXI. Investigations in Optics with special reference to the Spectroscope, *The London, Edinburgh and Dublin Philosophical Magazine and Journal of Science* 8 (49) (1879) 261-274. doi:10.1080/14786447908639684.

URL <http://dx.doi.org/10.1080/14786447908639684>

- [28] C. C. J. Pagani, D. S. Souza, M. A. F. Medeiros, Slat noise: Aeroacoustic beamforming in closed-section wind tunnel with numerical comparison, *AIAA Journal* 54 (7) (2016) 2100-2115. doi:10.2514/1.J054042.

URL <http://arc.aiaa.org/doi/abs/10.2514/1.J054042>

- [29] F. Scarano, Iterative image deformation methods in PIV, *Measurement Science and Technology* 13 (1) (2002) R1-R19. doi:10.1088/0957-0233/13/1/201.

URL <http://stacks.iop.org/0957-0233/13/i=1/a=201?key=crossref.1f47f7e3276cfd93e4e6338d0f5d3f18>

- [30] C. D. Meinhart, S. T. Wereley, The theory of diffraction-limited resolution in microparticle image velocimetry, *Measurement Science and Technology* 14 (7) (2003) 1047-1053. doi:10.1088/0957-0233/14/7/320.

URL <http://stacks.iop.org/0957-0233/14/i=7/a=320>

- [31] M. Raffel, C. Willert, J. Kompenhans, Particle Image Velocimetry, Experimental Fluid Mechanics, Springer, Berlin, Heidelberg, 2007. doi:10.1007/978-3-540-72308-0.  
URL [http://scholar.google.com/scholar?hl=en&btnG=Search&q=intitle:No+Title{#}0\\$\delimiter"026E30F\\$http://books.google.com/books?hl=en&lr={&}id=jbD12-yHbooC{&}oi=fnd{&}pg=PR7{&}dq=Particle+Image+Velocimetry{&}ots=T1sq0sf5mU{&}sig=gEvGBErY1oPK-uQr{ }BQgYjnsSpM\\$\delimiter"026E30F\\$http://books.google.com/books?hl=](http://scholar.google.com/scholar?hl=en&btnG=Search&q=intitle:No+Title{#}0$\delimiter)
- [32] F. F. J. Schrijer, F. Scarano, Effect of predictor–corrector filtering on the stability and spatial resolution of iterative PIV interrogation, Experiments in Fluids 45 (5) (2008) 927–941. doi:10.1007/s00348-008-0511-7.  
URL <http://link.springer.com/10.1007/s00348-008-0511-7>
- [33] B. Wieneke, PIV uncertainty quantification from correlation statistics, Measurement Science and Technology 26 (7). doi:10.1088/0957-0233/26/7/074002.  
URL <http://stacks.iop.org/0957-0233/26/i=7/a=074002>
- [34] C. Arce León, F. Avallone, S. Pröbsting, D. Ragni, PIV Investigation of the Flow Past Solid and Slitted Sawtooth Serrated Trailing Edges, in: 54th AIAA Aerospace Sciences Meeting, no. January, American Institute of Aeronautics and Astronautics, San Diego, California, 2016, pp. 1–15. doi:10.2514/6.2016-1014.  
URL <http://arc.aiaa.org/doi/10.2514/6.2016-1014>
- [35] Y. Guo, Aircraft Flap Side Edge Noise Modeling and Prediction, AIAA/CEAS Aeroacoustics Conference (17) (2011) 1–25. doi:10.2514/6.2011-2731.
- [36] R. Amiet, Noise due to turbulent flow past a trailing edge, Journal of Sound and Vibration 47 (3) (1976) 387–393. doi:10.1016/0022-460X(76)90948-2.

URL <http://www.sciencedirect.com/science/article/pii/S0022460X76909482>  
<http://linkinghub.elsevier.com/retrieve/pii/S0022460X76909482>

- [37] R. Parchen, Progress report DRAW: A prediction scheme for trailing-edge noise based on detailed boundary-layer characteristics, TNO Rept. HAGRPT-980023, TNO Institute of Applied Physics, The Netherlands.
- [38] M. Kamruzzaman, T. Lutz, On the Length Scales of Turbulence for Aeroacoustic Applications, AIAA Conference (June) (2011) 05 – 08.
- [39] O. Stalnov, P. Chaitanya, P. F. Joseph, Towards a non-empirical trailing edge noise prediction model, Journal of Sound and Vibration (2016) 1–19doi:10.1016/j.jsv.2015.10.011.  
URL <http://linkinghub.elsevier.com/retrieve/pii/S0022460X15008226>